Ceramics International xxx (xxxx) xxx

Contents lists available at ScienceDirect

Ceramics International

journal homepage: www.elsevier.com/locate/ceramint

In operando characterization of the ionic conductivity dependence on liquid transient phase and microstructure of cold-sintered Bi_2O_3-doped $Li_{1.3}Al_{0.3}Ti_{1.7}(PO_4)_3$ solid-state electrolyte

Andrés Mormeneo-Segarra [a,b], Sergio Ferrer-Nicomedes [a,b], Nuria Vicente-Agut [a,b,*], Antonio Barba-Juan [a,b]

[a] Department of Chemical Engineering, Universitat Jaume I, 12071, Castelló, Spain
[b] Institute of Ceramic Technology, Universitat Jaume I, 12071, Castelló, Spain

ARTICLE INFO

Handling Editor: Dr P. Vincenzini

Keywords:
Cold sintering process
Solid-ceramic electrolyte
Ionic conductivity
In *operando* impedance

ABSTRACT

A disruptive sintering technique, Cold Sintering Process (CSP), has been used to produce cold-sintered samples of Bi_2O_3-doped $Li_{1.3}Al_{0.3}Ti_{1.7}(PO_4)_3$ (LATP) as solid-state electrolyte (SSE). An *in operando* impedance study has been performed to shed light on this sintering process. In this work, Bi_2O_3 and 3 M acetic acid solution sintering aids were synergistically added to LATP powders to sinter at low temperature. Effects of Transient Liquid Phase (TLP) content on the sintering behavior, phase composition, microstructure, and electrochemical properties were all investigated for a LATP doped with 2 wt% Bi_2O_3 (optimal content) solid-state electrolyte (SSE). The data revealed that the final electrical properties, which are the key parameter decisive for their application, are defined by the following sintering parameters: Transient Liquid Phase (TLP) content, temperature, pressure, and dwell time. Using acetic acid 3 M as TLP, LATP-based samples can be cold-sintered at optimized sintering conditions of 150 °C and 700 MPa of uniaxial pressure for 90 min. The resultant SSE shows a high ionic conductivity ($4.5{\cdot}10^{-5}$ S cm^{-1}) at room temperature (RT) and relative density (~95%), which demonstrates the effectiveness of the low-temperature sintering process by optimizing the ionic conductivity of LATP-based SSE, also reducing preparation costs and CO_2 emissions.

1. Introduction

The world is currently facing major challenges at all levels, particularly in the energy sector, due to the depletion of fossil resources that have served as an energy source for centuries. Since the commercialization of lithium-ion batteries (LIBs) in 1991 by Sony Corporation [1], they have become the spearhead of the sector, owing to the effective utilization of renewable energy sources, alleviating the high demand for fossil fuels and the emission of CO_2 greenhouse gases [2,3]. Nevertheless, problems such as low energy density or safety issues due to the use of flammable organic liquid electrolytes [4], it is essential that conventional liquid electrolytes are replaced by solid electrolytes, it means to move to All Solid-State Batteries (ASSB) [5]. Non-flammable SSE can overcome most of the safety problems attributed to the use of organics electrolytes. In addition, their excellent chemical/electrochemical stability under extreme conditions and the ability to suppress the growth of lithium dendrites which cause fire or blast in the batteries due to short circuiting [6].

Up to now, a series of inorganic solid electrolytes have been studied, including LISICON-type ($Li_{3.75}Ge_{0.75}P_{0.25}O_4$) [7], NASICON-type [8–13], perovskite-type ($Li_{0.33}La_{0.557}TiO_3$) [14] or garnet-type ($Li_7La_3Zr_2O_{12}$) [15]. Goodenough was the first to report the NASICON-type solid-state electrolyte [16]. $Li_{1+x}Al_xTi_{2-x}(PO_4)_3$ was postulated as one of the most promising, among other like $Li_{1+x}Al_xGe_{2-x}(PO_4)_3$ or $LiHf_2(PO_4)_3$ [17]. LATP stands out from the rest due to its wide electrochemical window and good air stability, unlike most SSEs, which are hygroscopic and require an inert atmosphere for their manufacture, hindering the manufacturing process [18]. Furthermore, LATP presents the highest ionic conductivity of the grain (3 mS cm^{-1}) [19] measured at RT in the NASICON-type structure.

LATP powder can be synthesized from suitable precursors include in different ways as solid-state reaction [20], melt quenching [21], modified Pechini method [22], hydrothermal [23], sol-gel approaches [24], and co-precipitation [25]. The solid-state reaction is one of the most

* Corresponding author. Department of Chemical Engineering, Universitat Jaume I, 12071, Castelló, Spain.
E-mail address: vicenten@uji.es (N. Vicente-Agut).

https://doi.org/10.1016/j.ceramint.2023.08.333
Received 2 June 2023; Received in revised form 9 August 2023; Accepted 30 August 2023
Available online 31 August 2023

suitable approaches due to its simple preparation process. Pellets or green bodies are shaped from LATP powder, which are sintered (usually by conventional solid-state sintering) at temperatures between 700 and 1100 °C to maximize their ionic conductivities [26–30]. In some cases, sintering aids such as Li_2CO_3 [31], $LiBF_4$ [32], B_2O_3 [33], LiOH [34], LiCl [34], Li_3BO_3 [34], Li_3PO_4 [34], $LiBO_2$ [34] or Bi_2O_3 [35–37], are added to reduce sintering temperature or dwell time because of their low meting points. By the microstructural modification and a better densification lithium ions transport is promoted and grain boundary resistance reduced. Recently, Lee et al. used Bi_2O_3 sintering aid to reduce the sintering temperature of the LATP via LPS while simultaneously enhance its ionic conductivity [35].

To prevent the high energy consumption and pollutant gas emissions in conventional sintered LATP electrolytes (total ionic conductivity of ~1 mS cm^{-1}) because of high temperatures and long sintering times, a potential alternative, was proposed by Randall in 2016: the CSP [38]. This disruptive technique is based on a dissolution-precipitation process through a TLP, which dissolves the grain boundaries, facilitating the mass transport and thus sintering by precipitation. CSP can also use dopants to be dissolved in the TLP and, subsequently, precipitated at the grain boundaries again, improving properties such as ionic conductivity or relative density. Finally, it is especially noteworthy that CSP must work at temperatures below 300 °C and pressures of several hundred megapascals, resulting in less energy consumption and CO_2 emissions than conventional sintering [39]. CSP optimum conditions depend on powder characteristics (chemical composition, average particle size and particle size distribution), TLP nature and content, pressure, maximum temperature, and dwell time, which are intrinsic to each material. TLP nature and content seem to be one of the most relevant variables in the process, facilitating powder workability and its consolidation, but relationship between them determine the final microstructure of the cold-sintered bodies and therefore their electrical properties [40–45].

Vinnichenko [46] obtained LATP pellets via CSP at 200 °C, pressures between 510 and 600 MPa, 1 h at maximum temperature and 20% of H_2O or acetic acid as TLPs, yielding an ionic conductivity of $1.26{\cdot}10^{-5}$ and $8.2{\cdot}10^{-6}$ S cm^{-1}, respectively. Randall [47] obtained cold-sintered LATP at 130 °C, 620 MPa and 2 h of dwell time using 20% of DI water as TLP, resulting an ionic conductivity of $2.7{\cdot}10^{-5}$ S cm^{-1}. Other authors, in order to improve LATP properties, combined CSP with a post-annealing treatment increasing ionic conductivity up to ~$8{\cdot}10^{-5}$ S cm^{-1}. However, this procedure contravenes one of the bases of the CSP, which is to dramatically reduce the sintering temperature [48,49].

Recently, Hérisson de Beauvoir [50] has proposed a new *in situ* characterization technique to study the materials evolution during CSP of ZnO using acetic acid 1 M as TLP at 100 MPa of uniaxial pressure, three different temperatures (150, 200 and 250 °C) and a sintering time of 150 min. By *in situ* impedance characterization is possible to determine the optimal sintering conditions of the CSP and the implied mechanisms. This development brings key information about grain boundary formation at the solid/liquid interface, in terms of thermodynamic and kinetics. The role of the liquid phase is demonstrated in ZnO/acetic acid system allowing to follow the evolution of interfaces along sintering, offering a better control on the desired properties.

The aim of this work is to evaluate the TLP effect on cold-sintered Bi_2O_3-doped LATP pellets. Firstly, the optimal sintering conditions, uniaxial pressure, and temperature cycles for this material, were determined. To investigate the effects of TLP content (acid acetic) on the final properties of cold-sintered bodies (microstructure, relative density and, particularly, the ionic conductivity and activation energy) have been systematically studied by *in operando* EIS characterization and modelized by a proposed equivalent circuit. Furthermore, sintered LATP pellets prepared by CSP at 150 °C and 700 MPa using sintering aids and TLP have achieved a high ionic conductivity of up to $4.5{\cdot}10^{-5}$ S cm^{-1} with a relative density of ~95% and an activation energy of 0.351 eV. The microstructural analysis under TEM shows that the Bi_2O_3 particles are precipitated at the grain boundaries and TLP improves the microstructural homogeneity.

2. Materials and Methods

2.1. Preparation LATP powder

Al_2O_3 (Alfa Aesar, 99%), TiO_2 (Sigma-Aldrich, 99.8%), $NH_4(H_2PO_4)$ (Sigma-Aldrich, 99.99%) and Li_2CO_3 (Sigma-Aldrich, 99.99%) were used as raw materials in the LATP preparation via solid-state reaction method. Reactants were added stoichiometrically in agate jars to mix them via ball milling with zirconia balls and absolute ethanol as solvent in mass proportion 1:14:5 for 6 h. The mixture was dried in a vacuum oven at 80 °C for 12 h, after that, the calcination process was launched at 340 °C and 2 h of dwell time to remove the main organic impurities. The resultant powder was mixed manually with an agate mortar and placed in the furnace where solid-state reaction took place at 900 °C and 4 h of dwell time. The LATP resultant powder was ball-milled with the same proportions used in the first milling to get a good homogeneity. After collecting the milled LATP, it was dried with the same conditions mentioned previously to get the final LATP powder, Fig. S1(a) summarizes the experimental procedure used.

2.2. Pellets preparation

In order to upgrade the ionic conductivity of plain LATP, bismuth oxide (Alfa Aesar, 99.999%) was used as a flux that dissolves grain boundaries assisted by the acetic acid (HAc) 3 M (Alfa Aesar, 99,7%) as TLP for the CSP. Pellets were prepared with 2 wt% of Bi_2O_3 and different mass percentages of acetic acid (5, 10, 15, 20, 25 wt%), used as TLP in the CSP. First, Bi_2O_3 was dissolved in acetic acid, after which LATP was added to achieve proper homogenization. The resulting mixture was added to the mold and the process started. The sample was subjected to three deaerations and after that, the desired pressure (700 MPa) was reached and the thermal cycle was launched at 150 °C for 90 min. All the samples prepared in this study have a surface area of 76.51 mm^2 and a thickness of 1.35 ± 0.05 mm.

2.3. Electrochemical characterization

For *in operando* impedance measurements along the Cold Sintering Process of LATP solid-state electrolytes, a setup as shown in Fig. S1(b) was used, based on the system proposed by Hérisson de Beauvoir [50], also a schematic view of the setup is shown in Fig. S2(a). The system consists of a base, a piston, a concentric piece (all made of hardened steel) and a heating jacket that allows reaching the desired temperatures. However, in order to insulate both electrodes, Kapton film was used as an electrical isolator. With this setup it was possible to carry out the CSP as well as to measure simultaneously impedances along the process that has allowed to study the behavior of the samples during the process, being possible to understand the effect that the variables had on the final properties of the solid-state electrolyte obtained. Impedance measurements were performed potentiostatically at different temperatures within the frequency range of 1 MHz–10 Hz. A Multi Autolab M204 potentiostat from AUTOLAB equipped with an impedance module was employed.

2.4. Samples characterization

The cold-sintered samples obtained were characterized by XRD (Advance diffractometer, Bruker Theta-Theta, Germany), between 5 and 90°, SEM (FEG-SEM Quanta 200F) and TEM (Jem-2100 LaB6, JEOL) to study the changes that have occurred at microstructural level combined with the relative density (φ) measure which is the quotient between experimental and theorical density (Sartorius – YDK03). The theorical LATP density has been measured with a helium pycnometer resulting 2.91 g cm^{-3}, for calculating the experimental density by means of the

Archimedes' method with ethanol immersion, the samples were completely dried in an oven with silica gel for 1 h, weighed and left immersed in ethanol for another hour to achieve complete ethanol saturation. The samples were immersed again in the measuring device and the mass was registered, with both weights the density of the samples was determined.

3. Results and Discussion

As described in the **Materials and Methods** section of the present work, the influence of 3 M acetic acid as TLP content (5, 10, 15, 20 and 25 wt%) on the microstructure, relative density, and electrical properties (ionic conductivity and activation energy) has been studied. The CSP has been carried out at 150 °C, 700 MPa and 90 min for a LATP composition doped with 2 wt% Bi_2O_3. All samples were evaluated in duplicate, in 2 series.

The X-ray diffraction patterns of the cold-sintered samples with different TLP content and the pure LATP (ICSD 14585) [51] are shown in Fig. 1(a). An amplification can be found in Fig. 1(b), where α-Bi_2O_3 peaks reduced their intensity when TLP content increased, suggesting the partial formation of bismuth species, because of its dissolution in the TLP. The effect on the cold-sintered samples microstructure of the initial TLP content (between 0 and 25 wt%) is shown in Fig. 1(c-h), where white zones denote the bismuth species and the darker ones the LATP, highlighting how important TLP content is in CSP and how it works. SEM samples where fractured and no further treatment like polishing or heat treatment was applied because a microstructure change could take place [47,48,52]. Higher TLP contents (for instance, 27.5 wt%) resulted in a worsening workability as the mixture leaked from the mold, resulting in poorly shaped bodies that present an uncertain TLP content. Sample without TLP (0 wt%) shows several agglomerates (marked with a yellow line). It can be observed that the higher TLP content, the lower number of agglomerates. From 15 wt% TLP onwards the number of agglomerates decreased considerably until they were eliminated at 25 wt% of TLP, probably due to the better homogenization of the starting mixture. These agglomerates were formed by deformation and inhomogeneity when mixing particles of the starting powder and TLP to carry out the CSP. This reinforces the idea that a proper distribution of TLP is highly significant to ensure a well cold-sintered bodies showing proper final properties. In line with the basics of CSP, the optimum TLP content is reached when the particles are ideally not in contact, and the liquid occupies the entire porosity of the starting powder. Once this limit is exceeded, it is not possible to carry out the process because the wetting limit is exceeded [40].

TEM image of the cold-sintered body, with 25 wt% initial content of TLP, at 150 °C for 90 min, where some grain boundaries are pointed out with red lines for better viewing can be seen in Fig. 2(a). Whiter areas are bismuth-rich while darker areas correspond to LATP. Bismuth is

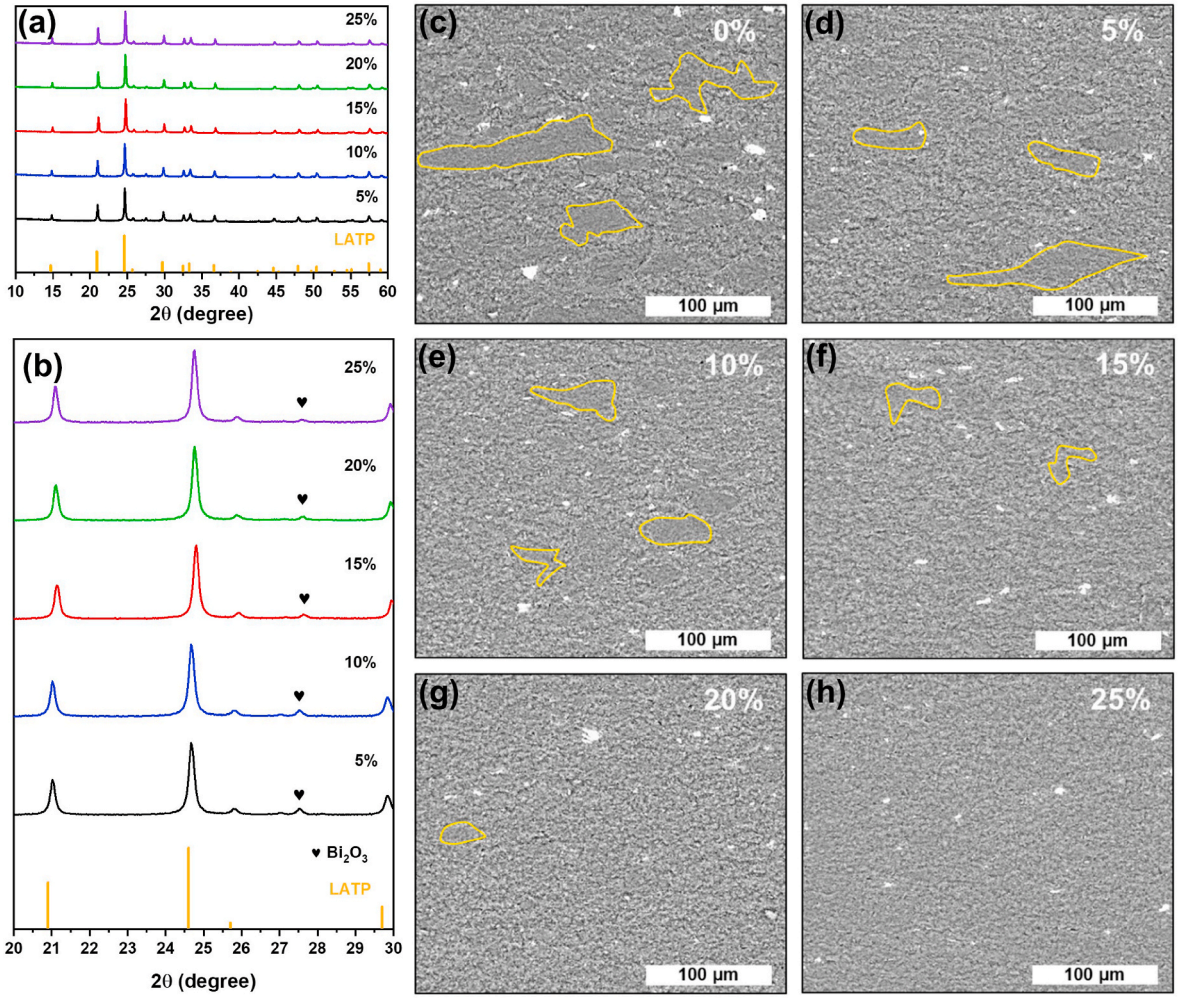

Fig. 1. (a) X-ray diffraction patterns of the cold-sintered pellets with different TLP content and the LATP database. (b) Amplification of the Bi_2O_3 peak at 27.5° showing the disappearance when increasing TLP content. (c–h) SEM images of the different TLP contents tested, denoting de decrease of the agglomerated zones (marked in yellow) within a major TLP content. (For interpretation of the references to colour in this figure legend, the reader is referred to the Web version of this article.)

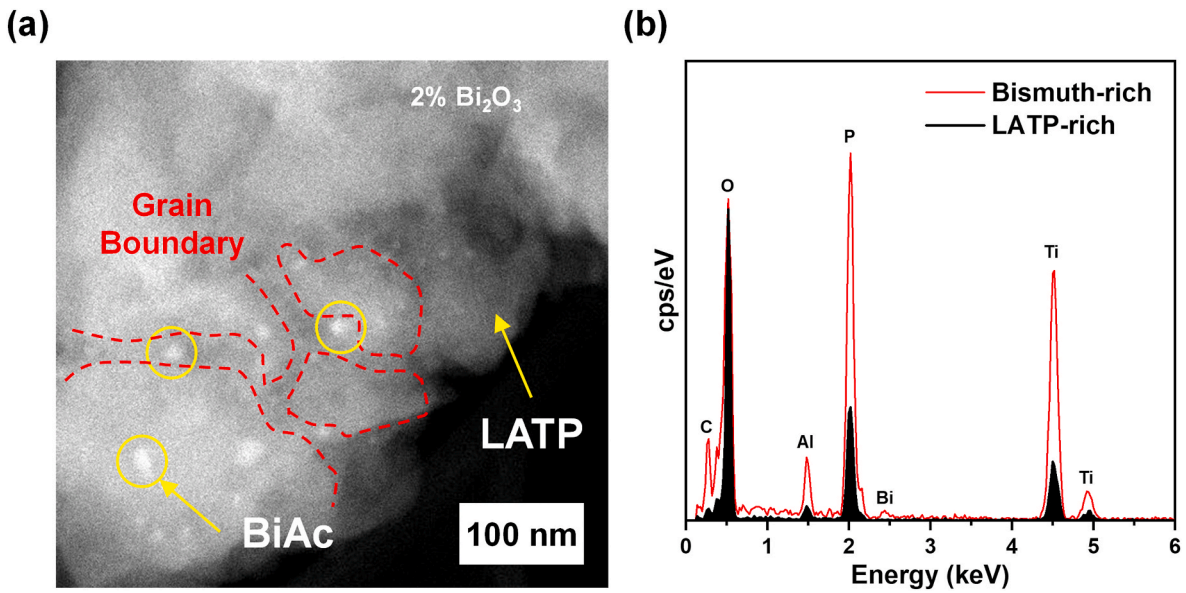

Fig. 2. (a) TEM image showing the bismuth acetate homogeneously distributed on the grain boundaries and (b) the EDX comparative of a bismuth-rich zone and an LATP-rich one where is visible the corresponding energy peaks of bismuth and carbon of the bismuth acetate in samples cold-sintered at 150 °C for 90 min (both samples were prepared by CSP using a 25 wt% of TLP).

homogeneously distributed along the grain boundary. Fig. 2(b) shows the comparative EDX spectra of the white and dark areas, showing Bi and C peaks and reinforcing the idea of bismuth acetate formation, which was introduced previously with XRD discussion. This behavior is due to the better dissolution of 2 wt% Bi_2O_3 as dopant in TLP as its content increases (authors have also studied the optimum content of Bi_2O_3 concluding the 2 wt% is the best option since their minima activation energy; the corresponding paper is pending publication).

The density of the samples can be considered virtually constant (ranges between 94.7 and 95.6% of the theoretical density), due to the high pressures used in the CSP, which highlights a high compaction of the particles, especially at the early stages of the CSP (heating step before reaching dwell temperature) [53,54].

The microstructural evolution of the CSP samples at different dwell times (0, 45 and 90 min) at maximum temperature (150 °C) and prepared with a 25 wt% of TLP is shown in Fig. 3(a-d). They show the progressive reduction of agglomerated zones until reaching the final microstructure, with a complete homogenization of the piece and the total suppression of the agglomerated zones due to the action of the TLP in the CSP. Analogously, a higher magnification of the microstructures corresponding to the green sample and to the sample cold-sintered at 150 °C for 90 min, are shown and no grain growth, typical at these conditions [38], and the elimination of initial small agglomerates can be observed (Fig. 3(e-f)). The microstructure of the green sample represents the starting point when no temperature has been applied and the maximum pressure has just been reached.

One of the most important characteristics for this type of SSE is the ionic conductivity, which is determined by impedance and subsequently modelled by means of a well-known Randle's equivalent circuit. Fig. S3 shows a typical impedance spectrum at RT of samples included in the present study, also displays the proposed equivalent circuit [55] used to quantify the electrical behavior of the SSE. The impedance plots consist of two well-defined parts: the high frequency semicircle related to grain boundary resistance and middle frequency diffusion pattern and an inclined line in response to the blocking layer. The equivalent circuit consisting of $(R_g)(R_{gb}CPE_1)(R_1\ CPE_2)C_1$. R_g, R_{gb}, CPE_1, and $(R_1\ CPE_2)C_1$ represent grain resistance, constant phase element, grain-boundary resistance, and elements which fits impedance related to Li + diffusion within the electrolyte, respectively.

Considering the above-mentioned findings, five SSE have been prepared according to the following initial content of TLP: 5, 10, 15, 20 and 25 wt%. Several EIS spectra for each SSE have been obtained *in operando* during the whole CSP. By fitting the equivalent circuit to the impedance data for different TLP content, it is found the R_g and R_{gb} values. The ionic conductivity can be calculated by the equation:

$$\sigma = \frac{L}{S \cdot R_{gb}} \quad (1)$$

where σ is the ionic conductivity, L is the thickness of the sample (1.35 ± 0.05 mm, virtually constant along the CSP once 150 °C are reached) and S the surface area (76.51 mm^2, constant).

Fig. 4(a) shows the spectra at different stages of CSP and Fig. 4(b) shows the corresponding magnification. Resistance increases during the stage at constant temperature of 150 °C due to the evaporation of the TLP. The ionic conductivity was calculated by equation (1) and plotted versus temperature in Fig. 4(c). The evolution of the ionic conductivity, calculated by equation (1), *vs.* CSP time for the five initial TLP content is shown in Fig. 4(d), where every curve corresponds to a TLP content tested, and each point of a curve corresponds to a spectrum registered *in operando* at a CSP time. All points shown in Fig. 4(d) have been replicated and the experimental results are shown in Fig. S4. The results in both series are coherent, verifying the reproducibility of CSP technique.

Three zones have been marked according to the CSP time in Fig. 4(d): the first area shows the heating step from RT up to 150 °C; in the second one, temperature remains constants at 150 °C; and the third one represents the cooling step from sintering temperature to RT. It should be pointed out that there is also a variation in the pressure over the CSP time: pressure increases up to 700 MPa and remains virtually constant while temperature also remains constant at 150 °C; during cooling step pressure decreases from 700 MPa to about 550 MPa. (For a better understanding, Fig. 4(d) can be visualized in conjunction with Fig. S2(b), which represents the pressure and temperature variation along the process). Fig. 4(d) provides following evidence:

1. In the five initial content of TLP tested it is remarkable that the initial ionic conductivity values (before starting CSP) are higher than the final ones (after ending CSP and returning to RT), likely due to the fact that before starting CSP, EIS measurements correspond to TLP.

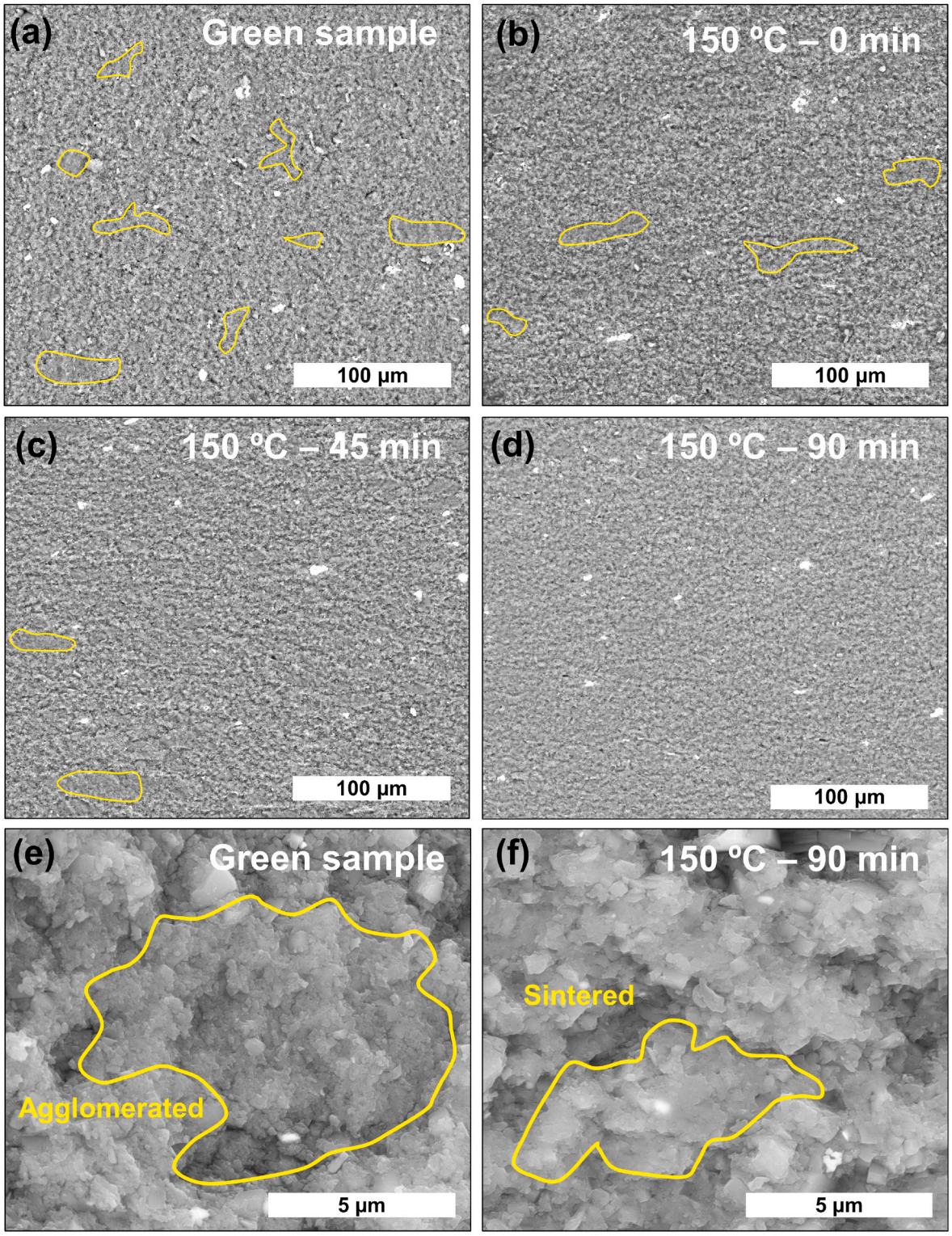

Fig. 3. (a–d) SEM images evolution of a cold-sintered sample prepared with a 25 wt% initial content of TLP: pressure cycle has been the same for four samples; no temperature cycle has been applied to green sample while the rest of images have been taken after the CSP at 150 °C and dwell times of 0, 45 and 90 min. (e–f) SEM images comparing the microstructure of the green sample and the cold-sintered one at 150 °C for 90 min (both samples were prepared by CSP using a 25 wt% of TLP). (For interpretation of the references to colour in this figure legend, the reader is referred to the Web version of this article.)

2. During dwell time at 150 °C, the ionic conductivity values gradually decrease until reaching a plateau which indicates that TLP is fully evaporated and, therefore, the CSP is over (For a better understanding, see Fig. S2(b) where pressure reaches the same kind of plateau at the same CSP times that the ionic conductivity). In a similar way, in the CSP time where temperature remains constant, the lower initial content of TLP the softer decrease in ionic conductivity, and therefore the samples with a higher initial content of TLP need longer time to reach this above-mentioned plateau: ~90 min for samples with 15, 20 and 25 wt% of TLP *vs.* ~60 min for samples with

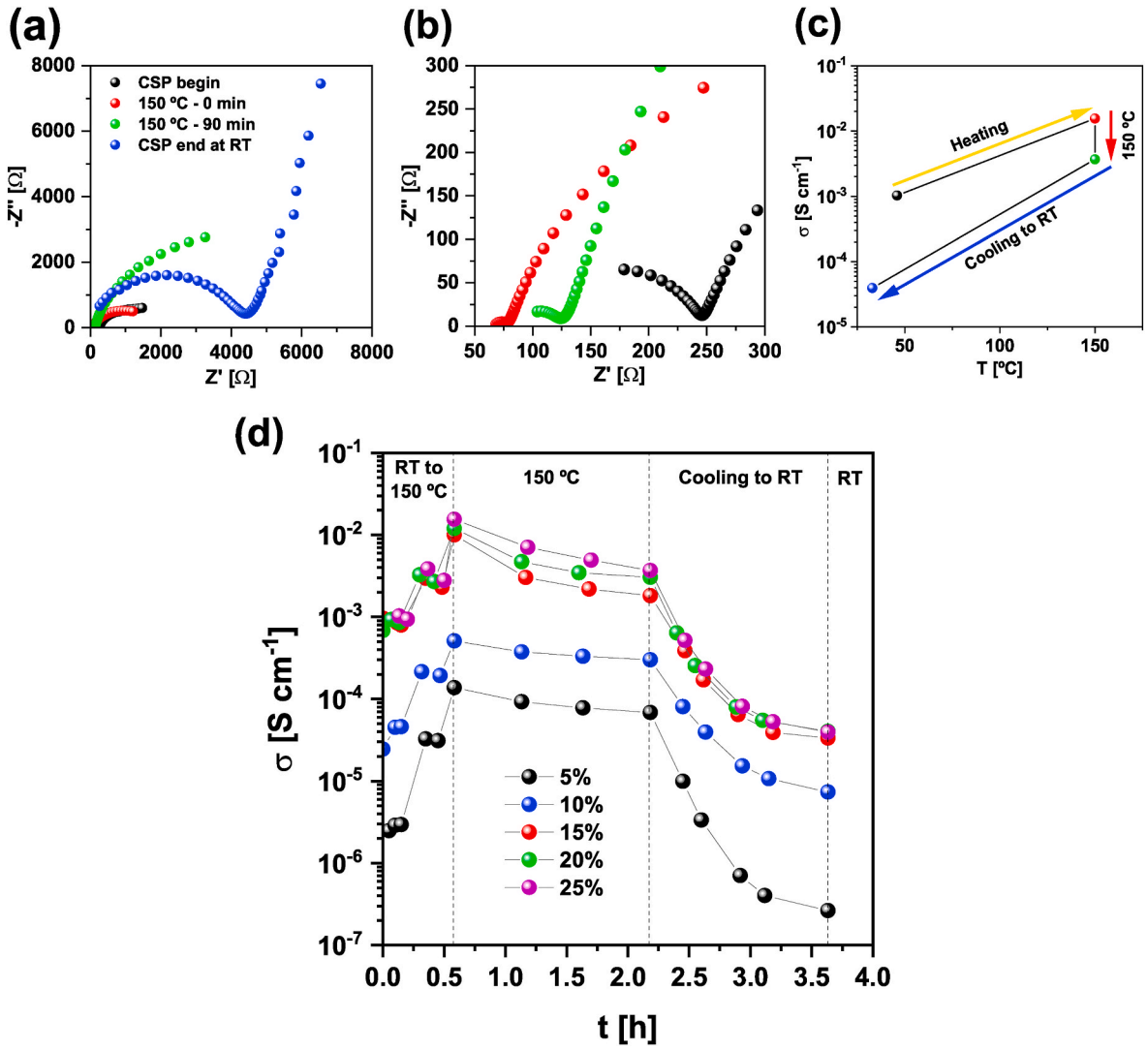

Fig. 4. (a) Impedance spectra at different times of the CSP for a sample with 25 wt% of TLP and 2% of Bi2O3, black dots refer to the first spectrum recorded at room temperature when the TLP is completely present in the sample. Red dots refer to the first spectrum recorded at maximum temperature (150 °C). Green dots denote the last spectrum at 150 °C and the blue dots represent the final spectrum at RT under pressure when CSP is completed. (b) Amplification of (a). (c) Ionic conductivity dependence on temperature along the CSP for a sample with 25 wt% of TLP and 2 wt% of Bi2O3. (d) Evolution of the ionic conductivity along the CSP time for the first series studied with different TLP contents (5, 10, 15, 20, 25 wt%). (For interpretation of the references to colour in this figure legend, the reader is referred to the Web version of this article.)

5 and 10 wt% TLP. This conclusion is also supported by SEM images of samples with 25 wt% initial content of TLP taken at 0, 45 and 90 min of dwell time at 150 °C (see Fig. 3(a–d)), where at the 0 min sinterization has not taken place yet, at 45 min the number of agglomerates has been reduced and at 90 min CSP has finished.

3. The cooling step by natural convection shows the clear dependence of the ionic conductivity on temperature.
4. Finally, the last dots denote the calculated ionic conductivity values at RT.

The ionic conductivity values for the present SSE obtained via CSP are higher than many of the obtained by conventional sintering at high temperatures for the same SSE [56–60].

As stated before, an important subject is the dependence of the ionic conductivity on temperature. When the CSP step at constant temperature is ended samples are cold-sintered and the decreasing ionic conductivity of samples during cooling step is due to the decreasing temperature. The relationship between conductivity and temperature follows the modified Arrhenius law in the form [61]:

$$\sigma \cdot T = A \cdot e^{-\frac{E_a}{k_B \cdot T}} \quad (2)$$

where A is the preexponential term, E_a the activation energy, k_B the Boltzmann constant and T the temperature. The ionic conductivity measurements were taken on the unit itself during the cooling process from 150 °C to RT, this is the reason why the measurements are not taken at the same exact temperature at each time as it depends on the cooling process measurements and these results cannot be plotted within its average of both series (For the same reason Fig. 4(d) and Fig. S4 showing the two replicate series cannot be included in only one figure. using mean values; however, it is possible to obtain a mean value at RT). The Arrhenius plot for series 1 is shown in Fig. 5(a) (Fig. S5(a) for series 2) together the calculated values for activation energy, which do not follow any clear relation with the initial content of TLP used in CSP: in fact, sample with 10 wt% initial content of TLP has the mean lowest activation energy (0.378 eV). Moreover, these findings also do not agree with the degree of sintering observed by SEM images shown in Fig. 1 (c–h). In order to explain this apparent random behavior, two considerations must be followed:

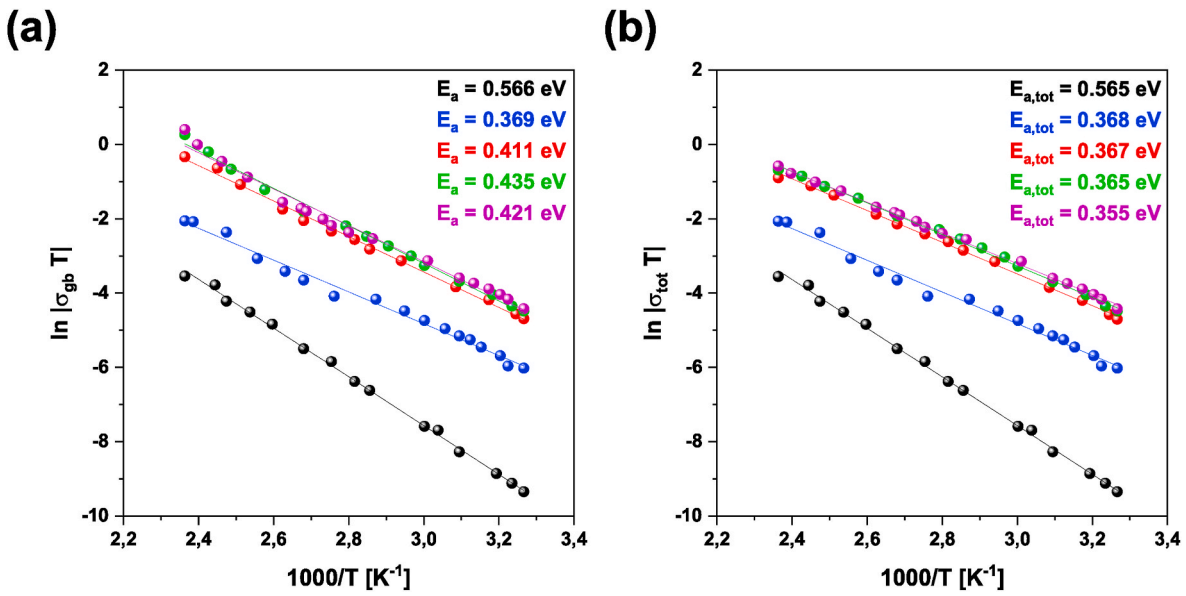

Fig. 5. (a) Arrhenius plot from equation (2) and (b) equation (4) for the different initial content of TLP used in CSP and their corresponding activation energies (experimental points range from 150 °C to RT) for the first series.

1. The right analysis of cooling step requires dividing it into three sections, because, simultaneously with the decrease in temperature, there is a slight drop in pressure (progressive and constant). These three sections of cooling step are summarized in Table S1: first section goes from 150 to 100 °C, WA of the sample inside the mold is zero and the absolute pressure is reduced due to the contraction produced by the decrease in temperature; in second and third sections, the SSE could adsorb water from air because the temperature is lower than the boiling point of water although the adsorbed water cannot be measured and quantified directly with the available equipment, but this is negligible for *in operando* impedance measurements. In order to study the influence of WA (when SSE are in equilibrium with air at different conditions of relative humidity and temperature inside a climate chamber) on ionic conductivity can be shown in Fig. S6. These results have been obtained for SSE with a 25 wt% initial content of TLP, results showed the same trend as in Yamada's [62] research, increasing the ionic conductivity with temperature and relative humidity higher than 60%. That confirms that, in the cold sintering process, it would be expected that since the tiny gap between punch and mold and highly densified pieces (~95%), the effect of get water absorption for sealed LATP samples is despicable compared to the percentage of relative humidity necessary for the effect on ionic conductivity to be appreciated. Hence, it was believed that the differences between the different stages of the process were not significant enough, that is, the activation energy was calculated taking into account the experimental points obtained during cooling step, when the sample was sintered, between 150 °C – RT.
2. Despite the slight decrease of the pressure along the CSP, the pressure values are always high enough (>550 MPa) to distort the LATP crystal network and reduce the mobility of the Li ion [63–65]. Then, ionic conductivity should be calculated not only from resistance of grain boundary but considering that total resistance of the sample is the sum of the grain and grain boundary resistances [66]. Then equation (1) must be rewritten as follows:

$$\sigma_{tot} = \frac{L}{S \cdot (R_{GB} + R_g)} \tag{3}$$

where σ_{tot} is the total ionic conductivity, L is the thickness of the sample, S the surface area and R_{gb} and R_g are the resistance of grain boundary and grain, respectively. Analogously, Arrhenius law must be rewritten as follows:

$$\sigma_{tot} \cdot T = A_{tot} \cdot e^{-\frac{E_{a,tot}}{k_B \cdot T}} \tag{4}$$

where A_{tot} is the pre-exponential term, $E_{a,tot}$ the total activation energy, k_B the Boltzmann constant and T the temperature. The Arrhenius plots obtained for series 1, using equation (4), can be found in Fig. 5(b) (Fig. S5(b) for series 2).

Table S2 and Table S3 show the values obtained for grain and grain boundary resistances from experimental points of cooling step until reaching RT, and the calculated values of ionic conductivity using equation (1) and total ionic conductivity using equation (3). It can be found that the values for the five initial content of TLP tested and for the two replicates (Series 1 and Series 2) follow the same trend: the grain resistance decreases when decreasing the temperature, contrarily to what might have been expected, and in the other hand, grain boundary resistance increases. This behavior can be explained with the modification of the unit cell parameters because of the high pressures applied, which result in a reduction of the ionic conductivity of the grain, thus increasing the grain's resistance. Therefore, as the temperature, and thus the pressure, decreases, the crystallite size increases and hence the ionic conductivity of the grain [63–65,67]. In order to graphically complement the previous information and the information provided in Fig. 4(d) and S4, where ionic conductivity has been plotted versus CSP time for five TLP content tested and for Series 1 and 2 respectively, Fig. S7 (a,b) shows the evolution of total ionic conductivity versus CSP time again for experiment series 1 and 2, respectively. The same trends can be observed in the four mentioned figures.

Fig. 6 shows the total ionic conductivity at RT and no pressure applied of cold-sintered bodies (SSE) and total activation energies *vs.* initial content of TLP. All points are the mean value of the two replicates. The values of each series and corresponding mean value are detailed in Table 1 and it can be seen how the ionic conductivity of the SSE increases with major initial content of TLP until it reaches a high ionic conductivity value of $4.0 \cdot 10^{-5}$ S cm^{-1} at 25 wt% initial content of TLP *vs.* the $2.7 \cdot 10^{-7}$ S cm^{-1} obtained with the 5 wt% initial content of TLP. There is a clear difference of more than two orders of magnitude between these two samples highlighting the dependence of the CSP, and the final properties, on the initial content of TLP. In this way, it is possible to evaluate the CSP by means of EIS *in operando*, allowing to

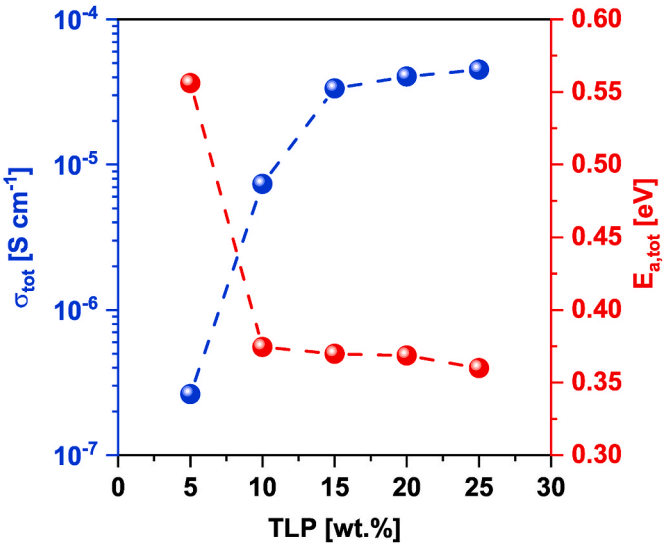

Fig. 6. Mean total ionic conductivities and activation energies for the different TLP contents studied.

Table 1
Ionic conductivities at RT for both series and its mean value at different TLP contents.

TLP [wt.%]	Series 1	Series 2	Average
	σ [S cm^{-1}]	σ [S cm^{-1}]	σ [S cm^{-1}]
5	$2.63{\cdot}10^{-7}$	$2.76{\cdot}10^{-7}$	$2.70{\cdot}10^{-7}$
10	$7.36{\cdot}10^{-6}$	$1.11{\cdot}10^{-5}$	$9.23{\cdot}10^{-6}$
15	$3.35{\cdot}10^{-5}$	$2.69{\cdot}10^{-5}$	$3.02{\cdot}10^{-5}$
20	$4.04{\cdot}10^{-5}$	$2.93{\cdot}10^{-5}$	$3.49{\cdot}10^{-5}$
25	$4.50{\cdot}10^{-5}$	$3.48{\cdot}10^{-5}$	$4.00{\cdot}10^{-5}$

know the optimal sintering points of temperature and time. The summary of the calculated values of activation energy using equations (2) and (4), and the corresponding mean values can be read in Table S4.

Comparing the values of E_a and $E_{a,tot}$, it can be concluded that: i) the grain resistance has a significant influence on the activation energy, and ii) the $E_{a,tot}$ values obtained agree with the microstructural description stated before as the lower the number of agglomerates, the higher the ionic conductivity, which results in the best $E_{a,tot}$ at 25 wt% of TLP. It is also possible to appreciate a notable decrease in the $E_{a,tot}$ of the samples with 15, 20 and 25 wt% TLP due to the fact that the resistance of the grain decreases as the temperature decreases, contrary to what happens with that of the grain boundary (see Table S2 and Table S3). This behavior can be attributed, as already indicated above, to the reduction in cell volume that occurs when high pressures are applied, decreasing the ability of the lithium ions to move and therefore the ionic conductivity is reduced: as an example, Fig. S8 compares the impedance spectra of the same sample at RT subjected to 560 MPa (pressure when the CSP finishes) and another at atmospheric pressure for a sample with 25 wt% of TLP and 2 wt% of Bi_2O_3, and it is observed that grain boundary resistance is reduced by removing the pressure due to the increased mobility of the lithium ion through the crystal lattice. In the case study, a pressure limit value of 900 MPa has also been verified, above which the crystal lattice is subjected to such a compression that it generates internal fractures causing the samples to break. It has been shown that, a certain pressure is necessary in order to consolidate a LATP pellet with good properties via CSP, but once obtained, a high stack pressure is not positive for the mobility of the lithium ions through the crystal lattice, thus reducing the ionic conductivity [68–70]. This is the reason why, as pressure is lost during cooling, the crystalline structures relax, changing the thickness of the grain boundary [66], and therefore its resistance, and decreasing that of the grain, as the lithium ions find it easier to move through the crystalline structure.

4. Conclusions

In this research, the dependence of the Bi_2O_3-doped $Li_{1.3}Al_{0.3}Ti_{1.7}(PO_4)_3$ pellets (densified via CSP at 150 °C, 90 min and 700 MPa) ionic conductivity on the TLP initial content has been studied with extraordinary results, a high ionic conductivity at RT ($4.5{\cdot}10^{-5}$ S cm^{-1}) and relative density (~95%), larger than others obtained via CSP and with conventional sintering at high temperatures. The CSP has been studied with *in operando* EIS measurements of the process been able to distinguish each part of the CSP and correlate it with the EIS spectrum by means of a corresponding equivalent circuit. This measurement technique allows to elucidate the different stages and variables that involve the CSP and the optimal values for each case, that can be found easily, as in this study with the best TLP content of acetic acid 3 M in the 25 wt%. Furthermore, with this procedure it has been possible to see the dependence of the ionic conductivity on CSP variables such as pressure, temperature and or time and explain the results with a great accuracy.

Declaration of competing interest

The authors declare that they have no known competing financial interests or personal relationships that could have appeared to influence the work reported in this paper.

Acknowledgements

This work has received funding from Generalitat Valenciana under Pla Complementari “Programa de Materials Avançats”, 2022 (grant number MFA/2022/030). A.B.-J. acknowledges the financial support from Ministerio de Ciencia e Innovación (Spain) grant number. MCIN/AEI/10.13039/501100011033. N.V.-A. acknowledges the support for the research from Universitat Jaume I under the grant number POSDOC/2020/04. A.M.-S. and S.F.-N. thank Generalitat Valenciana through FPI Fellowship Program (grant numbers ACIF/2020/294and ACIF/2021/050). The authors also acknowledge SCIC from UJI.

Supplementary Material

Supplementary Material with complementary information about experimental procedure and results is available in the online version of this article.

Appendix A. Supplementary data

Supplementary data to this article can be found online at https://doi.org/10.1016/j.ceramint.2023.08.333.

References

[1] Y. Li, M. Li, Z. Sun, Q. Ni, H. Jin, Y. Zhao, Recent advance on NASICON electrolyte in solid-state sodium metal batteries, Energy Storage Mater. 56 (2023) 582–599, https://doi.org/10.1016/J.ENSM.2023.01.047.
[2] D. Larcher, J.-M. Tarascon, Towards greener and more sustainable batteries for electrical energy storage, Nat. Chem. 7 (2015) 19–29, https://doi.org/10.1038/nchem.2085.
[3] B.C. Melot, J.-M. Tarascon, Design and preparation of materials for advanced electrochemical storage, Acc. Chem. Res. 46 (2013) 1226–1238, https://doi.org/10.1021/ar300088q.
[4] Y. Chen, K. Wen, T. Chen, X. Zhang, M. Armand, S. Chen, Recent progress in all-solid-state lithium batteries: the emerging strategies for advanced electrolytes and their interfaces. https://doi.org/10.1016/j.ensm.2020.05.019, 2020.
[5] M. Armand, P. Axmann, D. Bresser, M. Copley, K. Edström, C. Ekberg, D. Guyomard, B. Lestriez, P. Novák, M. Petranikova, W. Porcher, S. Trabesinger, M. Wohlfahrt-Mehrens, H. Zhang, Lithium-ion batteries – current state of the art and anticipated developments, J. Power Sources 479 (2020), 228708, https://doi.org/10.1016/J.JPOWSOUR.2020.228708.

[6] C.T. Love, O.A. Baturina, K.E. Swider-Lyons, Observation of lithium dendrites at ambient temperature and below, ECS Electrochem. Lett. 4 (2015) A24, https://doi.org/10.1149/2.0041502eel.
[7] T. Okumura, S. Taminato, Y. Miyazaki, M. Kitamura, T. Saito, T. Takeuchi, H. Kobayashi, LISICON-based amorphous oxide for bulk-type all-solid-state lithium-ion battery, ACS Appl. Energy Mater. 3 (2020) 3220–3229, https://doi.org/10.1021/acsaem.9b01949.
[8] J.A. Dias, S.H. Santagneli, Y. Messaddeq, Methods for lithium ion NASICON preparation: from solid-state synthesis to highly conductive glass-ceramics, J. Phys. Chem. C 124 (2020) 26518–26539, https://doi.org/10.1021/ACS.JPCC.0C07385/ASSET/IMAGES/LARGE/JP0C07385_0003.JPEG.
[9] H.D. Lim, J.H. Park, H.J. Shin, J. Jeong, J.T. Kim, K.W. Nam, H.G. Jung, K. Y. Chung, A review of challenges and issues concerning interfaces for all-solid-state batteries, Energy Storage Mater. 25 (2020) 224–250, https://doi.org/10.1016/J.ENSM.2019.10.011.
[10] P. Wu, W. Zhou, X. Su, J. Li, M. Su, X. Zhou, B.W. Sheldon, W. Lu, Recent advances in conduction mechanisms, synthesis methods, and improvement strategies for Li1 +xAlxTi2−x(PO4)3 solid electrolyte for all-solid-state lithium batteries, Adv. Energy Mater. 13 (2023), 2203440, https://doi.org/10.1002/AENM.202203440.
[11] C. Li, R. Li, K. Liu, R. Si, Z. Zhang, Y.-S. Hu, C. Zhizhen Zhang, NaSICON, A promising solid electrolyte for solid-state sodium batteries, Interdisciplinary Mater. 1 (2022) 396–416, https://doi.org/10.1002/IDM2.12044.
[12] Y. Ren, K. Chen, R. Chen, T. Liu, Y. Zhang, C.W. Nan, Oxide electrolytes for lithium batteries, J. Am. Ceram. Soc. 98 (2015) 3603–3623, https://doi.org/10.1111/JACE.13844.
[13] K. Yang, L. Chen, J. Ma, Y.-B. He, F. Kang, Progress and perspective of Li1 + xAlxTi2-x(PO4)3 ceramic electrolyte in lithium batteries, InfoMat 3 (2021) 1195–1217, https://doi.org/10.1002/INF2.12222.
[14] R. Lv, W. Kou, S. Guo, W. Wu, Y. Zhang, Y. Wang, J. Wang, Preparing two-dimensional ordered Li0.33La0.557TiO3 crystal in interlayer channel of thin laminar inorganic solid-state electrolyte towards ultrafast Li+ transfer, Angew. Chem. Int. Ed. 61 (2022), e202114220, https://doi.org/10.1002/anie.202114220.
[15] R. Inada, A. Takeda, Y. Yamazaki, S. Miyake, Y. Sakurai, V. Thangadurai, Effect of postannealing on the properties of a Ta-doped Li7La3Zr2O12 solid electrolyte degraded by Li dendrite penetration, ACS Appl. Energy Mater. 3 (2020) 12517–12524, https://doi.org/10.1021/acsaem.0c02474.
[16] J.B. Goodenough, H.Y.P. Hong, J.A. Kafalas, Fast Na+-ion transport in skeleton structures, Mater. Res. Bull. 11 (1976) 203–220, https://doi.org/10.1016/0025-5408(76)90077-5.
[17] J. Christopher Bachman, S. Muy, A. Grimaud, H.-H. Chang, N. Pour, S.F. Lux, O. Paschos, F. Maglia, S. Lupart, P. Lamp, L. Giordano, Y. Shao-Horn, Inorganic solid-state electrolytes for lithium batteries: mechanisms and properties governing ion conduction, Chem. Rev. 116 (2016) 140–162, https://doi.org/10.1021/acs.chemrev.5b00563.
[18] W. Xiao, J. Wang, L. Fan, J. Zhang, X. Li, Recent advances in Li 1+x Al x Ti 2−x (PO 4) 3 solid-state electrolyte for safe lithium batteries. https://doi.org/10.1016/j.ensm.2018.10.012, 2018.
[19] H. Aono, E. Sugimoto, Y. Sadaoka, N. Imanaka, G.-Y. Adachi, Ionic conductivity of solid electrolytes based on lithium titanium phosphate, J. Electrochem. Soc. 137 (1990) 1023–1027.
[20] Q. Yang, J. Huang, Y. Li, Y. Wang, J. Qiu, J. Zhang, H. Yu, X. Yu, H. Li, L. Chen, Surface-protected LiCoO2 with ultrathin solid oxide electrolyte film for high-voltage lithium ion batteries and lithium polymer batteries, J. Power Sources 388 (2018) 65–70, https://doi.org/10.1016/J.JPOWSOUR.2018.03.076.
[21] J. Fu, Superionic conductivity of glass-ceramics in the system Li 2O- Al 2O 3-TiO 2-P 2O 5, Solid State Ionics 96 (1997) 195–200, https://doi.org/10.1016/S0167-2738(97)00018-0.
[22] X. Xu, Z. Wen, X. Yang, L. Chen, Dense nanostructured solid electrolyte with high Li-ion conductivity by spark plasma sintering technique, Mater. Res. Bull. 43 (2008) 2334–2341, https://doi.org/10.1016/J.MATERRESBULL.2007.08.007.
[23] S. He, Y. Xu, B. Zhang, X. Sun, Y. Chen, Y. Jin, Unique rhombus-like precursor for synthesis of Li1.3Al0.3Ti1.7(PO4)3 solid electrolyte with high ionic conductivity, Chem. Eng. J. 345 (2018) 483–491, https://doi.org/10.1016/j.cej.2018.03.151.
[24] E. jeong Yi, K. young Yoon, H.A. Jung, T. Nakayama, M. jung Ji, H. Hwang, Fabrication and electrochemical properties of Li1.3Al0.3Ti1.7(PO4)3 solid electrolytes by sol-gel method, Appl. Surf. Sci. 473 (2019) 622–626, https://doi.org/10.1016/J.APSUSC.2018.12.202.
[25] S. Duluard, A. Paillassa, L. Puech, P. Vinatier, V. Turq, P. Rozier, P. Lenormand, P. L. Taberna, P. Simon, F. Ansart, Lithium conducting solid electrolyte Li1.3Al0.3Ti1.7(PO4)3 obtained via solution chemistry, J. Eur. Ceram. Soc. 33 (2013) 1145–1153, https://doi.org/10.1016/J.JEURCERAMSOC.2012.08.005.
[26] S. Wang, Y. Ding, G. Zhou, G. Yu, A. Manthiram, Durability of the Li1+xTi2–xAlx(PO4)3 solid electrolyte in lithium–sulfur batteries, ACS Energy Lett. 1 (2016) 1080–1085, https://doi.org/10.1021/acsenergylett.6b00481.
[27] K. Nagata, T. Nanno, All solid battery with phosphate compounds made through sintering process, J. Power Sources 174 (2007) 832–837, https://doi.org/10.1016/j.jpowsour.2007.06.227.
[28] K. Arbi, W. Bucheli, R. Jiménez, J. Sanz, High lithium ion conducting solid electrolytes based on NASICON Li1+xAlxM2−x(PO4)3 materials (M = Ti, Ge and $0 \leq x \leq 0.5$), J. Eur. Ceram. Soc. 35 (2015) 1477–1484, https://doi.org/10.1016/J.JEURCERAMSOC.2014.11.023.
[29] D.H. Kothari, D.K. Kanchan, Study of Study of electrical properties of gallium-doped lithium titanium aluminum phosphate compounds, Ionics 21 (2015) 1253–1259, https://doi.org/10.1007/S11581-014-1287-9/FIGURES/9.
[30] G. Yan, S. Yu, J.F. Nonemacher, H. Tempel, H. Kungl, J. Malzbender, R.-A. Eichel, M. Krüger, Influence of sintering temperature on conductivity and mechanical behavior of the solid electrolyte LATP. https://doi.org/10.1016/j.ceramint.2019.04.191, 2019.
[31] Y. Luo, H. Gao, X. Zhao, Insights into the sinterability and electrical properties of Li1.3Al0.3Ti1.7(PO4)3-(Li2CO3·Bi2O3) composite electrolytes, Ceram. Int. 48 (2022) 8387–8394, https://doi.org/10.1016/J.CERAMINT.2021.12.045.
[32] L. Dai, J. Wang, Z. Shi, L. Yu, J. Shi, Influence of LiBF4 sintering aid on the microstructure and conductivity of LATP solid electrolyte, Ceram. Int. 47 (2021) 11662–11667, https://doi.org/10.1016/J.CERAMINT.2021.01.004.
[33] W. Ślubowska, L. Montagne, O. Lafon, F. Méar, K. Kwatek, B2O3-Doped LATP glass-ceramics studied by X-ray diffractometry and MAS NMR spectroscopy methods, Nanomaterials 11 (2021) 390, https://doi.org/10.3390/NANO11020390, 11 (2021) 390.
[34] K. Waetzig, C. Heubner, M. Kusnezoff, Reduced sintering temperatures of Li+ conductive Li1.3Al0.3Ti1.7(PO4)3 ceramics, Crystals 10 (2020), https://doi.org/10.3390/cryst10050408.
[35] S.D. Lee, K.N. Jung, H. Kim, H.S. Shin, S.W. Song, M.S. Park, J.W. Lee, Composite electrolyte for all-solid-state lithium batteries: low-temperature fabrication and conductivity enhancement, ChemSusChem 10 (2017) 2175–2181, https://doi.org/10.1002/cssc.201700104.
[36] Y. Luo, H. Gao, X. Zhao, Insights into the sinterability and electrical properties of Li1.3Al0.3Ti1.7(PO4)3-(Li2CO3·Bi2O3) composite electrolytes, Ceram. Int. 48 (2022) 8387–8394, https://doi.org/10.1016/J.CERAMINT.2021.12.045.
[37] H. Leng, J. Nie, J. Luo, Combining cold sintering and Bi2O3-Activated liquid-phase sintering to fabricate high-conductivity Mg-doped NASICON at reduced temperatures, J. Materiomics 5 (2019) 237–246, https://doi.org/10.1016/J.JMAT.2019.02.005.
[38] J. Guo, H. Guo, A.L. Baker, M.T. Lanagan, E.R. Kupp, G.L. Messing, C.A. Randall, Cold sintering: a paradigm shift for processing and integration of ceramics, Angew. Chem. Int. Ed. 55 (2016) 11457–11461, https://doi.org/10.1002/ANIE.201605443.
[39] J.G. Pereira da Silva, M. Bram, A.M. Laptev, J. Gonzalez-Julian, Q. Ma, F. Tietz, O. Guillon, Sintering of a sodium-based NASICON electrolyte: a comparative study between cold, field assisted and conventional sintering methods, J. Eur. Ceram. Soc. 39 (2019) 2697–2702, https://doi.org/10.1016/J.JEURCERAMSOC.2019.03.023.
[40] M. Biesuz, G. Taveri, A.I. Duff, E. Olevsky, D. Zhu, C. Hu, S. Grasso, A theoretical analysis of cold sintering, Adv. Appl. Ceram. 119 (2020) 75–89, https://doi.org/10.1080/17436753.2019.1692173.
[41] S. Grasso, M. Biesuz, L. Zoli, G. Taveri, A.I. Duff, D. Ke, A. Jiang, M.J. Reece, A review of cold sintering processes, 115–143, https://doi.org/10.1080/17436753.2019.1706825, 2020.
[42] T. Yu, J. Cheng, L. Li, B. Sun, X. Bao, H. Zhang, Current understanding and applications of the cold sintering process, Front. Chem. Sci. Eng. 13 (2019) 654–664, https://doi.org/10.1007/S11705-019-1832-1/METRICS.
[43] A. Galotta, V.M. Sglavo, The cold sintering process: a review on processing features, densification mechanisms and perspectives, J. Eur. Ceram. Soc. (2021), https://doi.org/10.1016/j.jeurceramsoc.2021.09.024.
[44] J.P. Maria, X. Kang, R.D. Floyd, E.C. Dickey, H. Guo, J. Guo, A. Baker, S. Funihashi, C.A. Randall, Cold sintering: current status and prospects, J. Mater. Res. 32 (2017) 3205–3218, https://doi.org/10.1557/jmr.2017.262.
[45] A. Ndayishimiye, S.H. Bang, C.J. Spiers, C.A. Randall, Reassessing cold sintering in the framework of pressure solution theory, J. Eur. Ceram. Soc. 43 (2023) 1–13, https://doi.org/10.1016/J.JEURCERAMSOC.2022.09.053.
[46] M. Vinnichenko, K. Waetzig, A. Aurich, C. Baumgaertner, M. Herrmann, C.W. Ho, M. Kusnezoff, C.W. Lee, Li-ion conductive Li1.3Al0.3Ti1.7(PO4)3 (LATP) solid electrolyte prepared by cold sintering process with various sintering additives, Nanomaterials 12 (2022), https://doi.org/10.3390/NANO12183178.
[47] W. Lee, C.K. Lyon, J.H. Seo, R. Lopez-Hallman, Y. Leng, C.Y. Wang, M.A. Hickner, C.A. Randall, E.D. Gomez, Ceramic–salt composite electrolytes from cold sintering, Adv. Funct. Mater. 29 (2019), https://doi.org/10.1002/ADFM.201807872.
[48] Y. Liu, J. Liu, Q. Sun, D. Wang, K.R. Adair, J. Liang, C. Zhang, L. Zhang, S. Lu, H. Huang, X. Song, X. Sun, Insight into the microstructure and ionic conductivity of cold sintered NASICON solid electrolyte for solid-state batteries, ACS Appl. Mater. Interfaces 11 (2019) 27890–27896, https://doi.org/10.1021/acsami.9b08132.
[49] H. Cai, T. Yu, D. Xie, B. Sun, J. Cheng, L. Li, X. Bao, H. Zhang, Microstructure and ionic conductivities of NASICON-type Li1.3Al0.3Ti1.7(PO4)3 solid electrolytes produced by cold sintering assisted process, J. Alloys Compd. 939 (2023), 168702, https://doi.org/10.1016/J.JALLCOM.2023.168702.
[50] T. Hérisson De Beauvoir, P.-L. Taberna, P. Simon, C. Estournès, Cold Sintering Process characterization by in operando electrochemical impedance spectroscopy, J. Eur. Ceram. Soc. 42 (2022) 5747–5755, https://doi.org/10.1016/j.jeurceramsoc.2022.05.077.
[51] M. Pogosova, I. Krasnikova, A. Sergeev, A. Zhugayevych, K. Stevenson, Correlating structure and transport properties in pristine and environmentally-aged superionic conductors based on Li 1.3 Al 0.3 Ti 1.7 (PO 4) 3 ceramics, J. Power Sources 448 (2020), 227367, https://doi.org/10.1016/j.jpowsour.2019.227367.
[52] S.S. Berbano, J. Guo, H. Guo, M.T. Lanagan, C.A. Randall, Cold sintering process of Li1.5Al0.5Ge1.5(PO4)3 solid electrolyte, J. Am. Ceram. Soc. 100 (2017) 2123–2135, https://doi.org/10.1111/jace.14727.
[53] R. Floyd, S. Lowum, J.P. Maria, Instrumentation for automated and quantitative low temperature compaction and sintering, Rev. Sci. Instrum. 90 (2019), https://doi.org/10.1063/1.5094040.
[54] H. Guo, J. Guo, A. Baker, C.A. Randall, Hydrothermal-assisted cold sintering process: a new guidance for low-temperature ceramic sintering, ACS Appl. Mater. Interfaces 8 (2016) 20909–20915, https://doi.org/10.1021/acsami.6b07481.

[55] N. Vicente, M. Haro, G. Garcia-Belmonte, New approaches to the lithiation kinetics in reaction-limited battery electrodes through electrochemical impedance spectroscopy, Chem. Commun. 54 (2018) 1025, https://doi.org/10.1039/c7cc08373d.

[56] M. Zhang, J. Liu, W. He, Preparation, characterization and conductivity studies of Li1.3M0.3Ti1.7(PO4)3 (M = Al, Cr and Fe) glass–ceramics, Adv. Mater. Res. 602–604 (2013) 548–552, https://doi.org/10.4028/WWW.SCIENTIFIC.NET/AMR.602-604.548.

[57] H. Chen, H. Tao, X. Zhao, Q. Wu, Fabrication and ionic conductivity of amorphous Li–Al–Ti–P–O thin film, J. Non-Cryst. Solids 357 (2011) 3267–3271, https://doi.org/10.1016/J.JNONCRYSOL.2011.05.023.

[58] X. Ming Wu, S. Chen, F. Ren Mai, J. Hai Zhao, Z. Qiang He, Influence of the annealing technique on the properties of Li ion-conductive Li 1.3 Al 0.3 Ti 1.7 (PO 4) 3 films, (n.d.). https://doi.org/10.1007/s11581-012-0788-7.

[59] N. V Kosova, E.T. Devyatkina, A.P. Stepanov, A.L. Buzlukov, Lithium conductivity and lithium diffusion in NASICON-type Li 1+x Ti 2-x Al x (PO 4) 3 (x=0; 0.3) prepared by mechanical activation, (n.d.). https://doi.org/10.1007/s11581-007-0197-5.

[60] M. Schroeder, S. Glatthaar, J.R. Binder, Influence of spray granulation on the properties of wet chemically synthesized Li1.3Ti1.7Al0.3(PO4)3 (LATP) powders, Solid State Ionics 201 (2011) 49–53, https://doi.org/10.1016/J.SSI.2011.08.014.

[61] E. Barsoukov, J.R. (James R. Macdonald, Impedance Spectroscopy : Theory, Experiment, and Applications, third ed., Wiley, Hoboken, NJ, 2018, p. 207. https://www.wiley.com/en-us/Impedance+Spectroscopy%3A+Theory%2C+Experiment%2C+and+Applications%2C+3rd+Edition-p-9781119074083. (Accessed 25 April 2023).

[62] H. Yamada, N. Morimoto, H. Mukohara, T. Tojo, S. ichi Yano, E. Magome, T. Morimura, R. Bekarevich, K. Mitsuishi, Concerted influence of microstructure and adsorbed water on lithium-ion conduction of Li1.3Al0.3Ti1.7(PO4)3, J. Power Sources 511 (2021), https://doi.org/10.1016/j.jpowsour.2021.230422.

[63] A. La Monaca, G. Girard, S. Savoie, H. Demers, G. Bertoni, S. Krachkovskiy, S. Marras, E. Mugnaioli, M. Gemmi, D. Benetti, A. Vijh, F. Rosei, A. Paolella, Effect of pressure on the properties of a NASICON Li 1.3 Al 0.3 Ti 1.7 (PO 4) 3 nanofiber solid electrolyte †. https://doi.org/10.1039/d1ta01143j, 2021.

[64] T. Famprikis, Ö. Ulaş Kudu, J.A. Dawson, P. Canepa, F. Fauth, E. Suard, M. Zbiri, D. Dambournet, O.J. Borkiewicz, H. Bouyanfif, S.P. Emge, S. Cretu, J.-N. Chotard, C.P. Grey, W.G. Zeier, M. Saiful Islam, C. Masquelier, Under pressure: mechanochemical effects on structure and ion conduction in the sodium-ion solid electrolyte Na3PS4, J. Am. Chem. Soc. 142 (2020) 18422–18436, https://doi.org/10.1021/jacs.0c06668.

[65] Q. Chen, A. Braun, S. Yoon, N. Bagdassarov, T. Graule, Effect of lattice volume and compressive strain on the conductivity of BaCeY-oxide ceramic proton conductors, J. Eur. Ceram. Soc. 31 (2011) 2657–2661, https://doi.org/10.1016/J.JEURCERAMSOC.2011.02.014.

[66] Q. Xu, C.-L. Tsai, D. Song, S. Basak, H. Kungl, H. Tempel, F. Hausen, S. Yu, R.-A. Eichel, Insights into the reactive sintering and separated specific grain/grain boundary conductivities of Li 1.3 Al 0.3 Ti 1.7 (PO 4) 3, J. Power Sources 492 (2021), 229631, https://doi.org/10.1016/j.jpowsour.2021.229631.

[67] B. Davaasuren, F. Tietz, Impact of sintering temperature on phase formation, microstructure, crystallinity and ionic conductivity of Li1.5Al0.5Ti1.5(PO4)3, Solid State Ionics 338 (2019) 144–152, https://doi.org/10.1016/j.ssi.2019.05.016.

[68] A. Méry, S. Rousselot, D. Lepage, D. Aymé-Perrot, M. Dollé, Limiting factors affecting the ionic conductivities of LATP/polymer hybrid electrolytes, Batteries 9 (2023) 87, https://doi.org/10.3390/batteries9020087.

[69] H. Wang, M. Yu, Y. Wang, Z. Feng, Y. Wang, X. Lü, J. Zhu, Y. Ren, C. Liang, In-situ investigation of pressure effect on structural evolution and conductivity of Na3SbS4 superionic conductor, J. Power Sources 401 (2018) 111–116, https://doi.org/10.1016/J.JPOWSOUR.2018.05.037.

[70] M. Sara Jacob, N. Doddi, V. Shanmugam, G. Ebenezer Prasanna, M. Peddi, R. Vedarajan, S.B. Moodakare, R. Gopalan, Standardization of ionic conductivity measurements in Li1.3Al0.3Ti1.7(PO4)3-polymer composite electrolytes, Mater. Sci. Eng. B 286 (2022), 116049, https://doi.org/10.1016/J.MSEB.2022.116049.